Synthesis of Well-Defined, Surfactant-Free Co3O4 Nanoparticles

Pritchard, Jay; Morris, Louis; Walsh, Dominic; Sadasivan, Sajanikumari; Ménard, Hervé; Bellabarba, Ronan M.

Published in:
Catalysis Letters

DOI:
10.1007/s10562-017-2213-3

Publication date:
2018

Document Version
Peer reviewed version

Synthesis of well-defined, surfactant-free Co_3O_4 nanoparticles: The impact of size and manganese promotion on Co_3O_4 reduction and water oxidation activity

Jay Pritchard, [a] Louis Morris, [a] Dominic Walsh, [b] Sajanikumari Sadasivan, *[a] Hervé Ménard, [a] Ronan M. Bellabarba, [a] Mark T. Weller, [b] and Robert P. Tooze [a]

[a] *Sasol UK, Purdie Building, North Haugh, St Andrews, KY16 9ST, Scotland, UK.*

Tel: +44 (0)1334 460986

E-mail: sajanikumari@gmail.com

[b] *Department of Chemistry, University of Bath, Claverton Down, Bath, BA2 7AY, UK*

Abstract

A surfactant-free synthetic route has been developed to produce size-controlled, cube-like cobalt oxide nanoparticles of 3 different sizes in high yields. It was found that by using sodium nitrite as salt-mediating agent, near-quantitative yields could be obtained. The size of the nanoparticles could be altered from 11 nm to 22 nm by changing the cobalt concentration and reaction time. These surfactant-free nanoparticles form ideal substrates for facile deposition of further elements such as manganese. The effect of size of the cobalt oxide nanoparticles and the presence of manganese on the reducibility of cobalt oxide to metallic cobalt was investigated. Similarly, the effect of these parameters was investigated with a visible light promoted water oxidation system with cobalt oxide as catalyst, together with $[Ru(bpy)_3]^{2+}$ light harvester dye and an electron acceptor.

Keywords : cobalt oxide nanoparticles, manganese, reduction, water oxidation

Introduction

The preparation of shape-controlled monodisperse nanoparticles of metals and metal oxides[1] is of intense scientific and technological interest not only because of their potential as models for technical catalysts, but also for their possible direct application in catalysis and related areas such as photocatalysis, sensors and fuel cells.[2] Developments in the field allow nanoparticles with a well-defined size and shape to be synthesised,[3, 4] making them invaluable materials for both understanding mechanistic and structural aspects of catalysis [5, 6] and also offering the potential to design and synthesise novel, improved catalysts.[7, 8] Exquisite morphological control of nanoparticles can allow spectroscopic investigation of specific features or active sites.[4] Metal-support interactions can be investigated through deposition of nanoparticles onto supports,[9] and promoters can be studied through the synthesis of bimetallic nanoparticles,[10] or by adding the promoter to pre-synthesised nanoparticles. Generally, studying the effect that low levels of a promoter have on the behaviour of a metal oxide catalyst is difficult, since there are multiple factors at play; the strength of the interaction between metal oxide and the support,[11] the support used,[12] particle size, and dispersion.[13] It would be desirable to isolate variables and study them independently. The use of nanoparticles as model materials is one way of bridging this so called “materials gap”. Thus, nanomaterials offer the potential to advance our understanding of the complex and dynamic processes that occur during synthesis, activation, and catalysis.

Surfactants are routinely used to control the size and shape of colloidal nanoparticles. However, these organic stabilizers can block active surface sites of nanoparticles, are often expensive and sometimes toxic, limiting their use as model materials and in catalytic applications. The surfactant can be removed by calcination, but this can easily

modify the nanoparticles both chemically and physically for example by leaving residual carbon and/or modification of the shape/size of the nanoparticles.

Cobalt oxide is a widely used material, with important applications in lithium-ion batteries,[14] gas sensors,[15] and heterogeneous oxidation catalysis[16] amongst others. It can be reduced to metallic cobalt, the active phase in Fischer-Tropsch reaction for conversion of syngas to hydrocarbons.[17] Given the wide range of applications of cobalt oxide, surfactant-free synthesis of cobalt oxide nanoparticles is likely to have important implications in a variety of fields. There are very few reports in the literature on surfactant-free synthesis of well-defined cobalt oxide nanoparticles. Micron sized surfactant-free cobalt oxide has been synthesised via cobalt hydroxide as an intermediate.[18] Lestera *et al*. synthesised surfactant-free cobalt oxide nanoparticles on large scale using continuous-flow hydrothermal reactor.[19]

We were thus intrigued to read of a salt-mediated synthesis for the preparation of cobalt oxide nanocubes[20] in the size range of 10 nm to 25 nm, but in our hands the yields were unsatisfactorily low. We now report on a modification of this method which allows the preparation of cobalt oxide nanoparticles in high yields. The method can be optimised to give three different nanoparticle sizes, allowing the impact of size on the reduction of cobalt oxide to metal to be investigated. Also, since the surface of the nanoparticles is surfactant-free, other elements can be deposited on the surface of the cobalt oxide nanoparticles very easily. We have deposited manganese as a model promoter on the surface of cobalt oxide nanoparticles. The promotion of cobalt Fischer-Tropsch catalysts with manganese oxide is known to be an effective way of increasing selectivity to heavier hydrocarbons and decreasing methane selectivity,

whilst increasing the olefin to paraffin ratio.[21] For Fischer-Tropsch reaction, cobalt oxide is reduced to the active metallic Co, hence it is crucial to understand the impact of the presence of manganese has on this reduction process. Previous studies have investigated this effect for titania[22]/silica[23,24]/carbon[25] supported cobalt oxide system wherein the location of manganese could be on the support and/or cobalt oxide. The metal/promoter-support interaction also plays a role in the reduction process. Herein we have manganese specifically on the cobalt oxide nanoparticle and have excluded any contribution from the support by investigating an unsupported cobalt oxide system. Hence in the current work, we specifically investigate the impact of manganese on the reduction process when MnO_x is on cobalt oxide. We further investigated the effect of manganese on water oxidation activity of cobalt oxide.

2. Experimental

2.1 Synthesis of cobalt oxide nanoparticles

Cobalt oxide nanocubes were synthesised by a modified surfactant-free literature method.[20]

To synthesise 22 nm cobalt oxide nanoparticles, NaOH (2.4 g, 60 mmol, Fischer >99 % purity) and $NaNO_2$ (150 g, 2.174 mol, Aldrich >99 % purity) were dissolved in 100 ml water. The solution was heated to 105 °C with stirring, and air was bubbled through the solution at approximately 100 ml/min. After 30 minutes at 105 °C, 20 ml of 2 M $Co(NO_3)_2 \cdot 6H_2O$ solution (Aldrich >98 % purity) was injected over 150 seconds. On contact with the NaOH/$NaNO_2$ solution, the pink cobalt nitrate solution turned blue, then cloudy pink on further addition and mixing. The precipitate then rapidly turned pale brown. The production of NO_x gasses led to some foaming on the surface which

diminished with time. The reaction mixture turned black after four hours, but it was left for a further two hours to ensure completion of reaction before cooling.

The same procedure was used to synthesise 16 nm particles, but in this case 20 ml of 3 M $Co(NO_3)_2 \cdot 6H_2O$ was used and the amount of NaOH was accordingly adjusted to 3.6 g (90 mmol). The amount of sodium nitrite was unchanged, at 150 g. After two hours, the brown precipitate had turned black, but the reaction was left for a further 4 hours before cooling.

The same procedure as for the 16 nm particles was used for the 11 nm nanoparticles, but the reaction time was reduced. Thus, 20 ml of 3 M $Co(NO_3)_2 \cdot 6H_2O$ was injected to the NaOH (3.6 g)/$NaNO_2$ (150 g) solution and the reaction was stopped after 3 hours instead of 6 hours.

In each case, the solid was recovered by centrifugation (7000 rpm, 7 min), removal of the supernatant, followed by washing and centrifugation (7800 rpm, 8 min) three times each; first with distilled water, then 18 % HCl, and finally distilled water again. The first wash with HCl resulted in some NO_x evolution (decomposition of residual nitrite and nitrogen containing reaction intermediates not removed by water) and a pink supernatant (cobalt solution). After the final wash with water, the supernatant was colourless with a pH of ~7. The products were dried overnight in a vacuum oven at 60 °C.

2.2 Synthesis of manganese modified cobalt oxide nanoparticles

To deposit manganese on cobalt oxide nanoparticles, aqueous $Mn(NO_3)_2 \cdot 4H_2O$ solutions of different concentrations **(Table 1)** were made by dilutions of a common

stock solution (10 ml, 0.40 mol/L). Cobalt oxide nanoparticles (100 mg) were dispersed in 4 ml distilled water by sonication, and 1 ml of $Mn(NO_3)_2{\cdot}4H_2O$ solution of the required concentration was added. The dispersion was heated to 60 °C on a rotary evaporator under atmospheric pressure, and subsequently dried using a rotary evaporator at 60 °C and 160 mbar for 1 hour, followed by 100 mbar for 1 hour. The product after solvent removal was then dried at 60 °C for 3 hours in a vacuum oven and then calcined at 250 °C for 6 hours with a 1 °C/min heating ramp in a muffle furnace. A similar protocol was used to prepare a control Mn-free sample whereby no manganese nitrate solution was added after dispersion of the nanoparticles in water.

Table 1: Manganese loadings used to prepare Mn-Cobalt oxide, and the manganese nitrate solutions used to obtain these.

Manganese loading / %wt	**Concentration $Mn(NO_3)_2{\cdot}4H_2O$ (aq) / mol L^{-1}**	**Mn:Co atomic ratio**
0	0	0
0.89	1.63×10^{-2}	0.013
1.76	3.27×10^{-2}	0.026
3.47	6.53×10^{-2}	0.052
10.00	0.203	0.163

2.3 Characterisation of nanoparticles

To determine sodium levels (from the mediating salt), a representative nanoparticle sample was sent to Butterworth Laboratories Ltd. UK for ICP analysis.

Temperature programmed reduction (TPR) was performed on a Micromeritics Autochem II 2950 chemisorption analyser connected to a Thermostar Mass Spectrometer. Samples of approximately 15 mg were heated to 120 °C under argon to flush out moisture and air, then cooled to 0 ° C before being heated to 700 ° C at a rate of 10 °C/min under a stream of 10 % H_2/Ar. X-ray diffractograms were obtained using a PANalytical X'Pert Pro diffractometer with a Co anode. Samples were scanned from 20° to 100° 2 theta at step time of 300 secs/scan. Transmission electron microscopy (TEM) was conducted on a Jeol JEM 2011 HRTEM at the University of St Andrews. Samples were dispersed in ethanol by sonication and a drop placed on carbon coated copper grid for analysis. Zeta-potential measurements were performed using Malvern Zetasizer Nano ZS at University of Bristol, UK. Aqueous solutions of cobalt oxide nanoparticles were prepared by dispersing 5 mg of nanoparticles in 5 mL of water by sonication for 10 mins prior to measurements.

X-ray photoelectron spectra were recorded on the KRATOS Axis Ultra DLD, with the analyser operating at the fixed pass energy of 160 eV for the survey spectrum and 20 eV for the individual regions. The measurements were carried out using the Al Kα monochromated source. Due to the nature of the materials, neutralisation was necessary during the acquisition. All of the spectra presented in this report have been corrected in energy using the position of adventitious carbon (C 1s) at 284.4 eV. All the samples were mounted as loose powders in a crucible sample holder. On average ~10 mg of material was used for each measurement.

2.4 Water oxidation of manganese modified cobalt oxide

Nitrogen degassed de-ionised water was used to prepare an acetate buffer of pH 5.2 (50 mM sodium acetate adjusted with acetic acid). A custom made glass 50 ml flask

was taken and 120 mg of $[Co(NH_3)_5Cl]Cl_2$ (98 %) electron acceptor and 45 mg $[Ru(bpy)_3]Cl_2 \cdot 6H_2O$ (99.95 %) sensitizer added together with 30 ml of buffer. The reaction flask was covered with foil to shield from light before 10 mg of cobalt oxide nanoparticles suspended in a further 5 ml of the degassed buffer was added. The light shielded reaction flask was then left stirring for 25 minutes to allow the electron acceptor to fully dissolve and the system to equilibrate.

The light shield covering was then removed and the stirred flask illuminated by royal blue LED (3 W, 120 lumen, λ max 450 - 460 nm) held at a distance of 2 cm from the edge of the reaction flask. This generated a measured output of average 10 mW/ cm^2 between 422-499 nm (Solartech Inc. Solar Meter 9.4), at the reaction flask (with measured LED light exposed surface area of 30.8 cm^2). O_2 release was monitored using a calibrated Vernier O_2-BTA O_2 gas sensor (of +/- 0.01-0.005 % resolution) fitted into the flask aperture and reactions in air were conducted in the flask (zeroed after equilibration). Onset of O_2 release usually occurred within 5 min after light on and was monitored for 90 minutes. The amount of O_2 gas released into the known headspace volume was calculated from measured O_2 levels. On illumination the pH of the buffered reaction mixtures increased (due to release of ammonia from the electron acceptor) from ~pH 5.2 to ~8.1 to 8.6 (depending on sample) at the 90 min end point. Replicate measurements were made for each sample, minor fluctuations in profiles marking onset and cessation of individual water oxidation cycles were obtained, but the overall patterns were very similar. O_2 output was consistent to within 6 % for each replicate and representative profiles plotted on graphs shown. Control experiments in the absence of light or added catalyst gave no measurable O_2 output. Control experiments in the absence of light or electron acceptor gave no measurable O_2 output. In absence

of metal oxide catalyst a low yield was obtained after a prolonged lag period (~30 mins) due to conversion of some decomposed $[Ru(bpy)_3]^{2+}$ light sensitizer dye into ruthenium oxide which then acts as a catalyst.[26] The maximum net O_2 generated, averaged production rate at t=5 to 15 min and maximum rate observed for 180 s was determined for all the samples as shown in **Table 2**. The turnover frequency (TOF) at maximum O_2 rate and quantum yield (ϕ) were calculated as shown below and example calculations are shown in Supplementary Information.

TOF = mol O_2 / mol of Co per sec (at the initial linear O_2 generation period).

Quantum yield (at 45 min) $\Phi O_2\%$ = O_2 produced at t = $O_{2(@45min)}$µmol/photons absorbed at t = 45 min × 400% (4 photons absorbed per O_2).

3. Results and Discussion

3.1 Synthesis and size control of cobalt oxide nanoparticles

Initial attempts at producing surfactant free cobalt oxide nanocubes using the literature procedure resulted in very low yields in our hands.[20] By replacing sodium nitrate in the reported synthesis with sodium nitrite, excellent yields of cobalt oxide nanocubes (~95 %) were obtained. TEM images showed the morphology of the product to be cube-like with an average particle size of around 22 nm (σ = 5.0 nm) **(Figure 1a).** HRTEM of the nanoparticle **(Figure 1b)** showed d spacing of 0.28 nm corresponding to the (220) plane of Co_3O_4. Powder X-Ray diffraction **(Figure 2a)** indicated pure Co_3O_4 (JCPDS file no 00-043-1003) with an average particle size of 22 nm as calculated by Scherrer equation. ICP analysis showed that the samples before washing were contaminated with sodium salts (0.37 wt %) but after washing with aqueous hydrochloric acid and water, sodium amount reduced to below detection limits (>0.01 wt %).

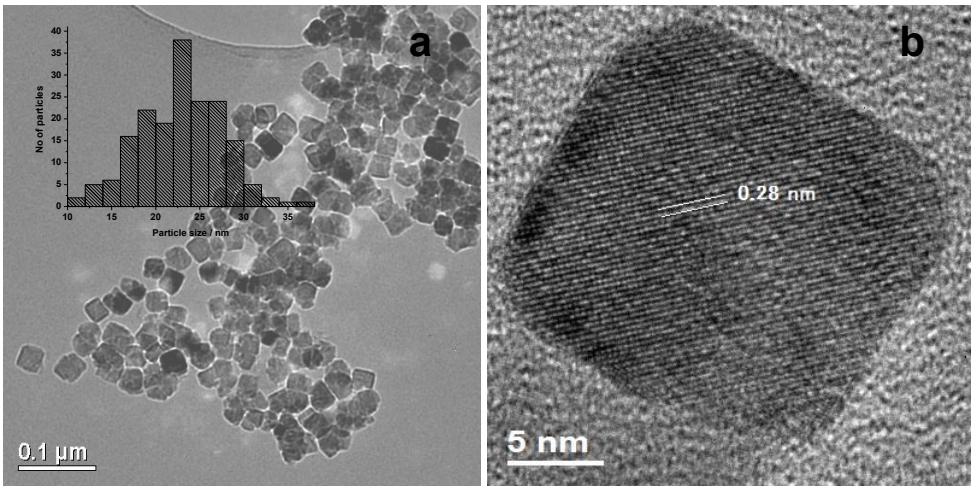

Figure 1: (a) Low magnification TEM and (b) HRTEM micrographs of as synthesised 22 nm Co_3O_4 nanoparticles. Inset in (a) showing particle size distribution.

The average crystallite size of the nanoparticles could be controlled by varying the concentration of cobalt nitrate solution. Increasing the cobalt nitrate concentration to 3 M instead of 2 M, resulted in substantial volumes of NO_x gas being evolved, causing the solution to foam slightly and fill the reaction vessel with brownish red gas. The production of NO_x gas was observed for about 2 hours after injection before subsiding. Increasing the cobalt concentration also increased the rate of reaction; the black product formed within 2 hours when using 3 M cobalt nitrate but took 4 hours when using 2 M cobalt nitrate. The particle size was found to be 16 nm, both by XRD and by TEM (σ = 3.7 nm) **(Figure 2b and Figure 3a, b).** This decrease in size with increase in cobalt nitrate concentration can be attributed to an increase in the rate of nucleation. This leads to the formation of larger number of nuclei and consequently formation of larger number of small particles. Further increase in cobalt nitrate concentration to 4 M did not affect the particle size significantly.

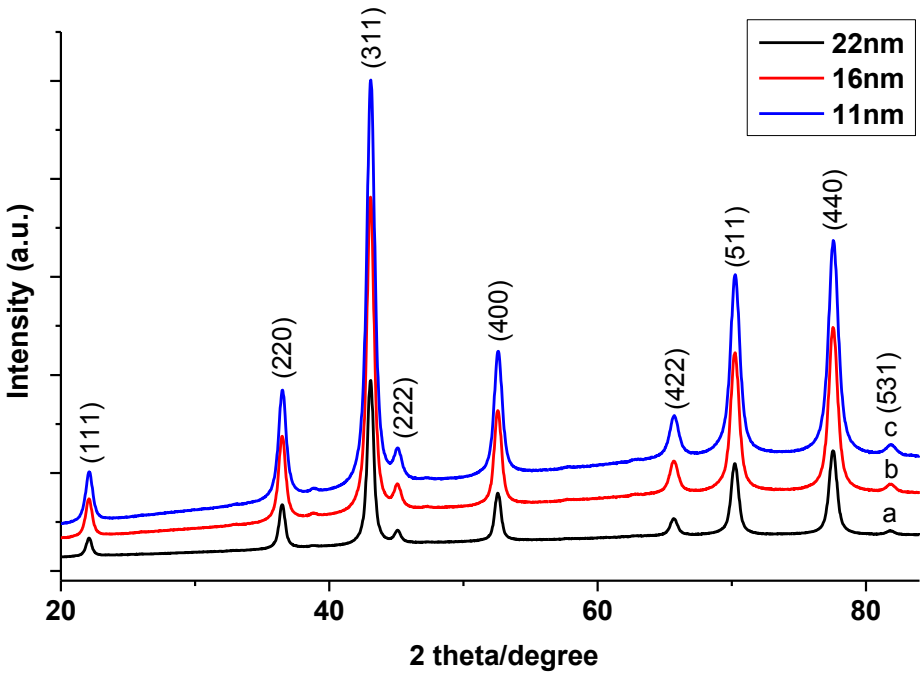

Figure 2: Powder X-ray diffractograms of surfactant free Co_3O_4 nanoparticles.

Keeping the concentration of cobalt nitrate at 3 M, the reaction was stopped at 3 hours instead of 6 hours. XRD **(Figure 2c)** confirmed the particles were pure Co_3O_4 with an average particle size of 11 nm. TEM images again showed cube-like cobalt oxide nanoparticles with an average size of 11 nm (σ = 2.9 nm) and d spacing corresponding to Co_3O_4 **(Figure 3 c, d)**. Decreasing the time from 6 hours to 3 hours decreased the yield to 80.8%. The presence of pink coloured solution on washing the sample with HCl indicated presence of cobalt intermediates. In a similar salt-mediated synthesis, Feng et al.[20] reported the presence of intermediates like cobalt(II) hydroxide nitrate and cobalt(II)-cobalt(III) hydrotalcite species. Presumably, in our case on increasing the reaction time these intermediates convert to Co_3O_4 and also add onto the existing cobalt oxide cubes resulting in an increase in particle size from 11 nm to 16 nm.

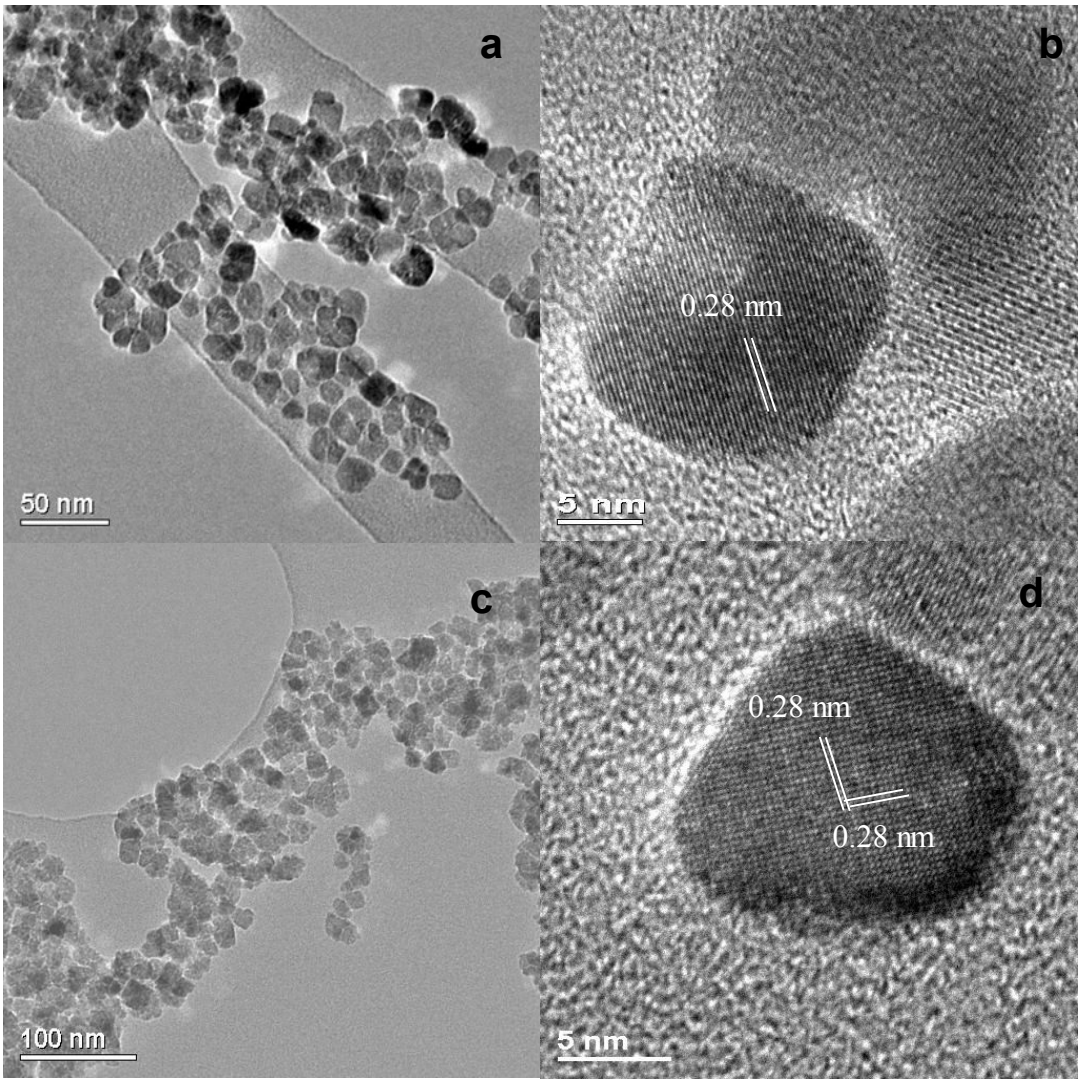

Figure 3: Low magnification TEM and HRTEM micrographs of as synthesised 16 nm (a,b) and 11 nm (c,d) Co_3O_4 nanoparticles.

3.2 Temperature programmed reduction (TPR) study of cobalt oxide nanoparticles

The above cobalt oxide nanoparticles with an average size of 11 nm, 16 nm and 22 nm were subjected to TPR to study the effect of crystallite size on reducibility. In general, the cobalt oxide nanoparticles show two main peaks **(Figure 4)** corresponding to the reduction of Co_3O_4 to CoO and CoO to Co.[27] The relative broadness of the second peak compared to the first peak indicates that the first step

of conversion of Co_3O_4 to CoO is fast, while the reduction of CoO to Co is more difficult.[28]

Comparison of the TPR profiles of cobalt oxide with different particle sizes shows that the peaks occur at a lower temperature for small particles than for large ones, indicating that small particles are quickly reduced than large ones. Previous TPR studies on unsupported cobalt oxide nanoparticles have seen a similar effect.[29] The specific surface area of the nanoparticles is higher for small nanoparticles, that is, the surface area to volume ratio for each nanoparticle is much higher. Hence, a relatively large proportion of the cobalt oxide in a sample of small nanoparticles is directly exposed to the hydrogen atmosphere, and can be reduced easily, whilst in the large particles, a relatively large amount of the cobalt oxide is in the core of the nanoparticles, where reduction is slower. Also, for the larger particles, the diffusion of hydrogen, water and lattice oxygen to the oxide-metal interface may be more difficult, further slowing reduction.

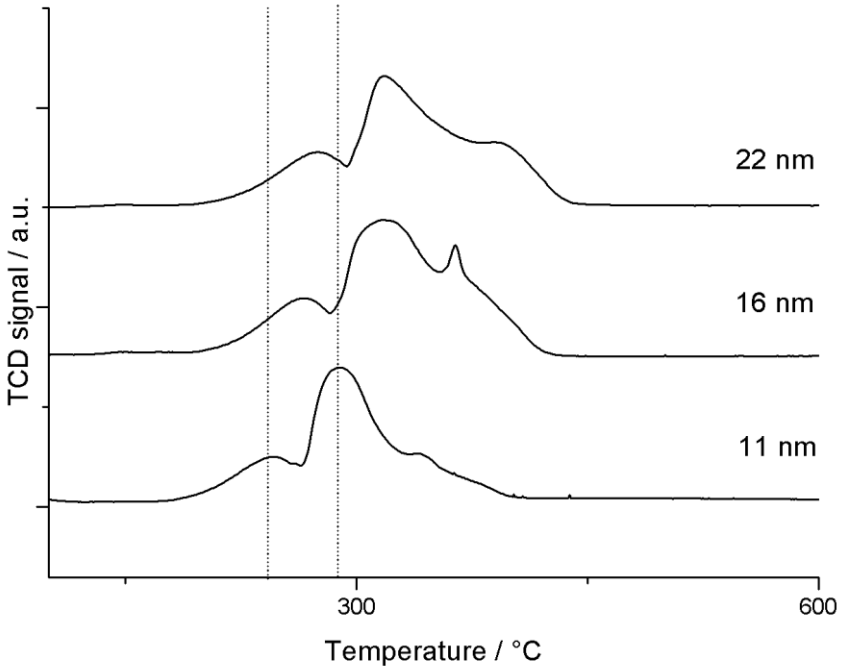

Figure 4 : TPR profiles of cobalt oxide nanoparticles with different sizes.

This relationship between particle size and the ease of reducibility follows the opposite trend to that generally observed in conventional supported catalysts, where reducibility is dominated by interaction between the nanoparticles and the support. In the supported catalyst system, small particles have a stronger interaction with the support, therefore they are more difficult to reduce.[30]

3.3 Manganese modified cobalt oxide nanoparticles: Synthesis and characterisation

The above surfactant-free nanoparticles having a negative zeta-potential at pH 7 (-29.6 mV for the 16 nm particle) are ideal materials for deposition of salts of promoter elements via dispersion in aqueous media. To demonstrate this we deposited manganese nitrate on the 16 nm cobalt oxide nanoparticles and studied the effect of Mn doping on the reducibility of cobalt oxide nanoparticles after calcination.

The manganese loading was varied from 0.9 wt % to 10 wt %. X-ray diffractograms did not detect manganese containing phases, and the Co_3O_4 reflections did not shift when manganese was incorporated **(Figure 5a).** Even at the highest manganese loading, only Co_3O_4 was detected by X-ray diffraction. The average crystallite size of Co_3O_4 did not change significantly after the deposition of manganese and calcination. The reflections did decrease in intensity with increasing manganese loading. Whilst there are reports in the literature where this was assigned to a decrease in the crystallinity of the sample[22] in this case, it was due to fluorescence of manganese under the cobalt X-ray source. This was confirmed by repeating the experiment under an iron X-ray source without significant variation in peak intensity (data not shown). The lack of any detectable manganese phase by XRD suggests that this is relatively amorphous or that it is does not form particles with long range crystalline order. Formation of very small, well dispersed particles, a thin layer, or a non-crystalline mixed oxide with the cobalt are all possible explanations.

The sample with the highest manganese loading (10 wt %) was analysed by TEM **(Figure 5b, c).** The nanoparticles retained their morphology, and did not sinter during calcination. The mean particle size and distribution remained similar after manganese impregnation and calcination. However, even at 10 wt% Mn loading, lack of contrast between Co and Mn made it difficult to distinguish between the two elements, although EDX **(Figure 5b, Inset)** confirmed the presence of Mn in the sample. HRTEM showed d spacing of 0.46 nm, 0.28 nm and 0.24 nm corresponding to the (111), (220) and (311) planes, respectively of Co_3O_4.

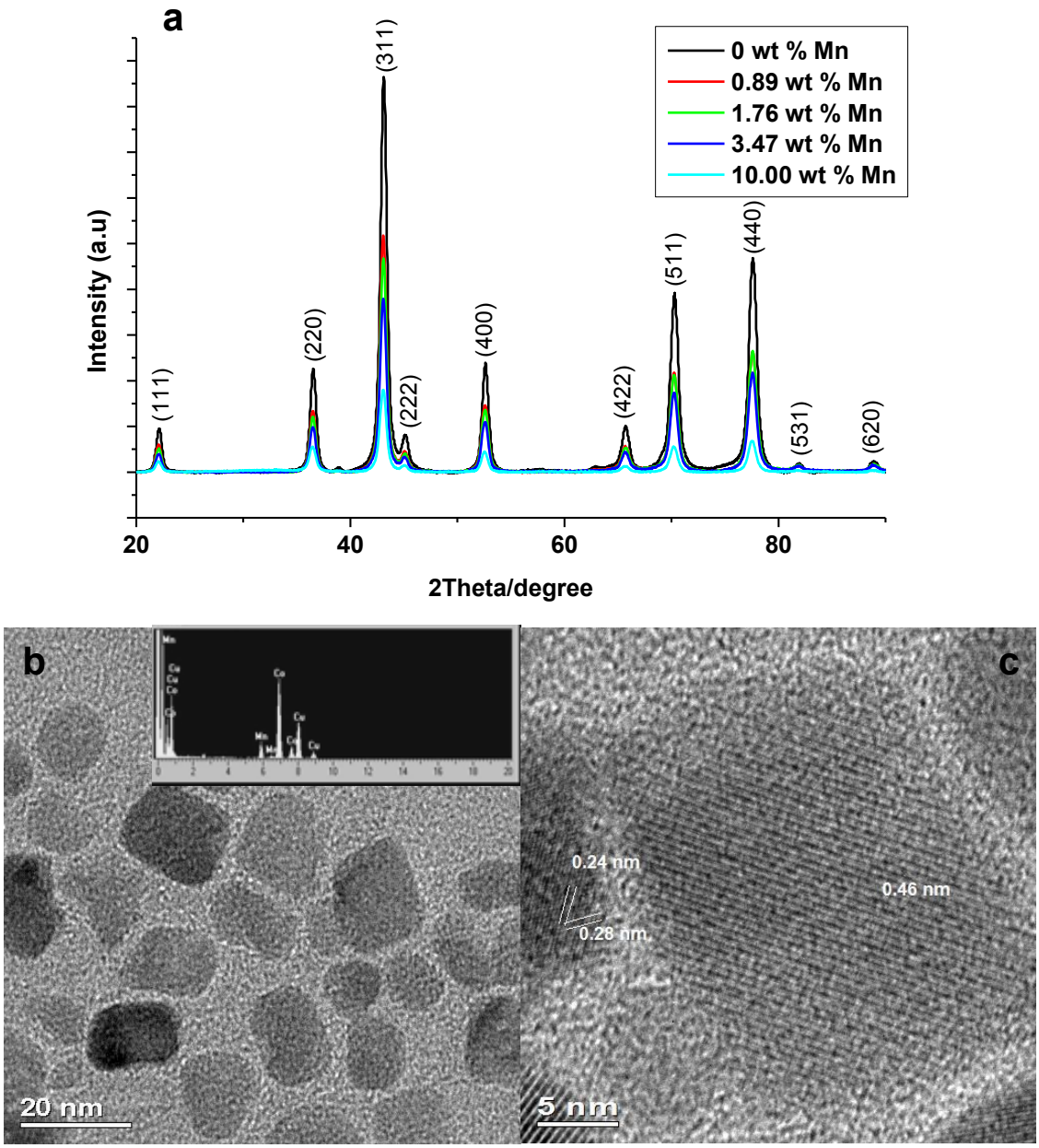

Figure 5: (a) X-ray diffractograms of the Co_3O_4 nanoparticles with different manganese loadings, (b) low magnification TEM and (c) HRTEM micrograph of cobalt oxide nanoparticle after modification with manganese (10 wt %). Inset in (b) showing EDX analyses for the nanoparticles.

The Mn modified cobalt oxide samples were further characterised by XPS. The increasing addition of manganese not only affects the intensity **(Figure 6a)** but also

results in a slight broadening of the Co 2p envelope. Although not observed by XRD, this broadening in the XPS could indicate the presence of a mixed oxide Mn-Co surface species while the bulk of the particle remain typical of Co (II, III) oxide (Co_3O_4).[31] For all the samples the XPS Mn 2p envelopes have a profile typical of Mn_2O_3 **(Figure 6b)**. The position in binding energy of the Mn $2p_{5/2}$ main component is found too low in energy for MnO_2 to be present as a majority species. The absence of a satellite peak at 646.0 eV also rules out the presence of MnO. The Mn 2p/Co 2p ratio shows a linear relation as a function of the bulk atomic ratio for the entire loading range (Figure 6c). This linear trend clearly states the growth mode remains constant. Assuming a surface density of 10 Mn atom/nm^2, [32] (i.e. equivalent to the number of Mn atoms required to achieve a monolayer coverage on a surface) a one monolayer of manganese oxide would be expected to theoretically produce a Mn/Co bulk atomic ratio of ~0.082. The linear correlation seen on both sides of this point confirms the exclusive formation of manganese oxide clusters on the cobalt oxide particles and not a monolayer like manganese oxide growth.

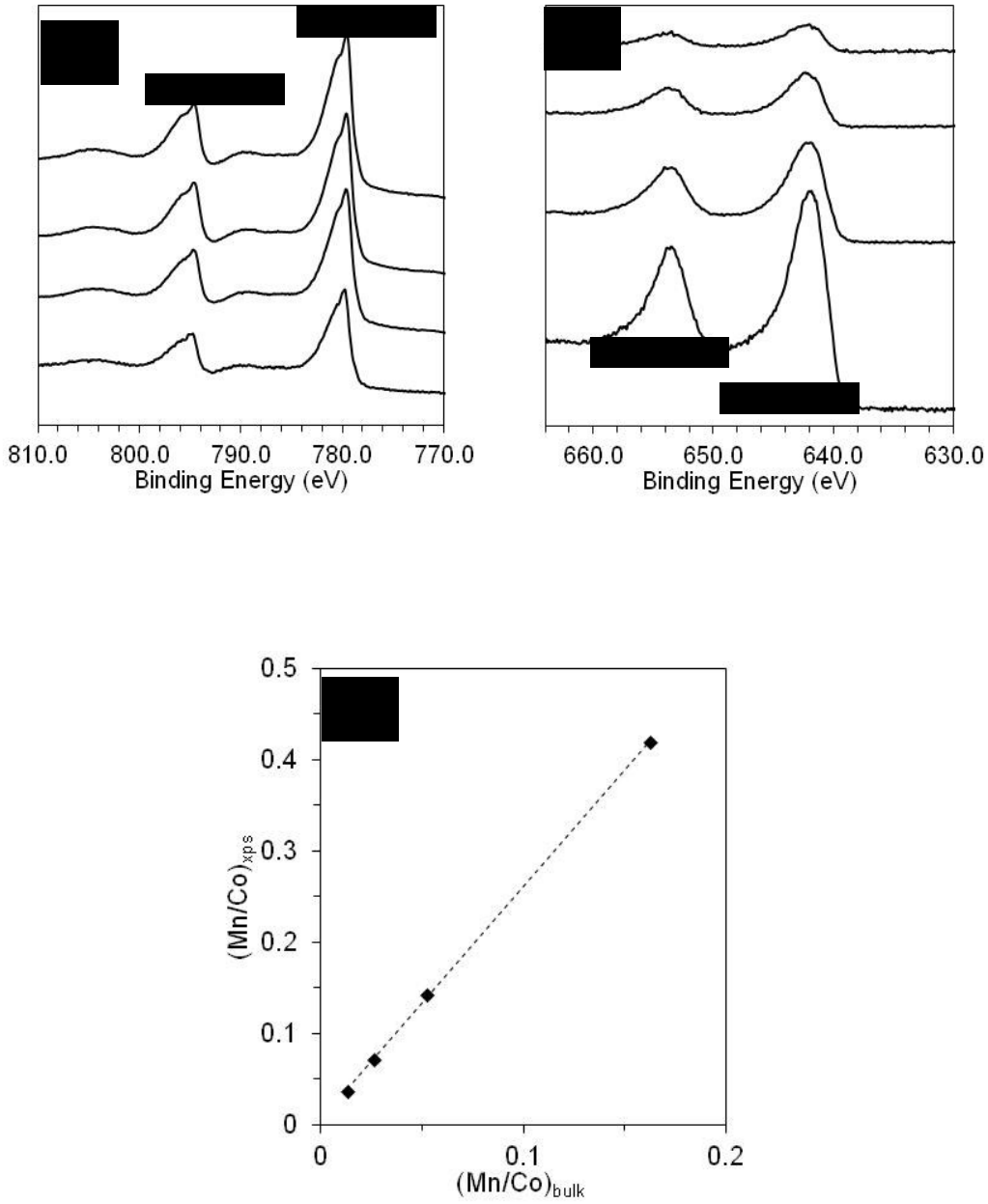

Figure 6: (a) XP Co 2p spectra, (b) XP Mn 2p spectra of the Co3O4 nanoparticles with from top to bottom: Mn 0.89 wt.%, Mn 1.76 wt.%, Mn 3.47 wt.% and Mn 10.00 wt.%. c) Experimental Mn 2p/Co 2p XPS peak area ratio $(Mn/Co)_{xps}$ as a function of the bulk atomic metal ratio $(Mn/Co)_{bulk}$.

By considering the XRD and XPS data together, we suggest that after calcination, Mn (III) oxides are mainly formed. This species is very well dispersed in the form of

small clusters and some of it could be in the form of a mixed Co-Mn oxide at the interface, hence it is not visible by XRD. Mixed Co-Mn spinels can form when Co^{3+} in the octahedral sites of the lattice, are substituted by Mn^{3+}. This model suggested by XPS and XRD is compatible with the difficulty in observing any discrete Mn based particles or domains by TEM. A similar conclusion was reached by Morales et. al. [33] and others,[34] who used XRD, STEM-EELS and EXAFS to characterise a $MnCo/TiO_2$ catalyst.

3.4 TPR of manganese modified cobalt oxide nanoparticles

Addition of manganese to a supported cobalt Fischer-Tropsch catalyst is reported to suppress the reducibility of cobalt oxide due to the formation of mixed Co-Mn spinel species, which are relatively difficult to reduce.[31,35] Herein we investigated the effect of manganese on unsupported cobalt oxide nanoparticles (size 16 nm) without the complications of the presence of support. TPR profiles of samples with different manganese loadings are shown in **Figure 7**. The first reduction peak (~ 265 °C) corresponding to the reduction of Co_3O_4 to CoO was not affected by low Mn loading of 0.89 wt%. With further increase in Mn loading the reduction temperature increased from 280 °C for 1.76 wt% Mn loading to 295 °C for 10 wt% Mn loading. The reduction of CoO to Co was affected more significantly by manganese even at low loadings. The addition of 0.89 wt% manganese shifted the peaks corresponding to the reduction $CoO \rightarrow Co^{(0)}$ (~315 °C) by ~30 °C higher in temperature compared to a Mn free sample and this increased with further increase in Mn loading. This significant effect on the second reduction peak compared to the first peak could be due to strong interaction between CoO and MnO.[24] Mn_2O_3 can be reduced to MnO above temperatures of 325 °C.[36]

The effect of Mn on the first and/or second reduction step has not been conclusive in reported literature and has been dependent on the preparation method. Some studies report that the CoO → $Co^{(0)}$ reduction peak broadened and shifted to higher temperatures, whilst the Co_3O_4 → CoO peak did not shift to higher temperatures when Mn was added.[24] Others report that both reduction steps were made more difficult via "encasement" of Co_3O_4 by manganese oxides and the formation of Mn-Co spinels.[37] [38] Regalbuto et al.[38] showed that when manganese has been selectively adsorbed onto cobalt oxide in a titania supported cobalt system, at low loading (0.03 wt% MnO), Mn helps in the reduction of cobalt oxide whereas at higher loading, Mn makes the reduction of both steps difficult. Similarly, Ahmad et al.[35] have shown that for low loading of Mn up to 1.5 wt%, Mn lowers the reduction temperature of cobalt oxide. All of these studies were carried out on supported manganese-cobalt oxide systems where the metal-support and/or promoter-support interaction can influence the reduction profile. Our results show that when manganese oxide is exclusively deposited on cobalt oxide, it affects both the reduction processes.

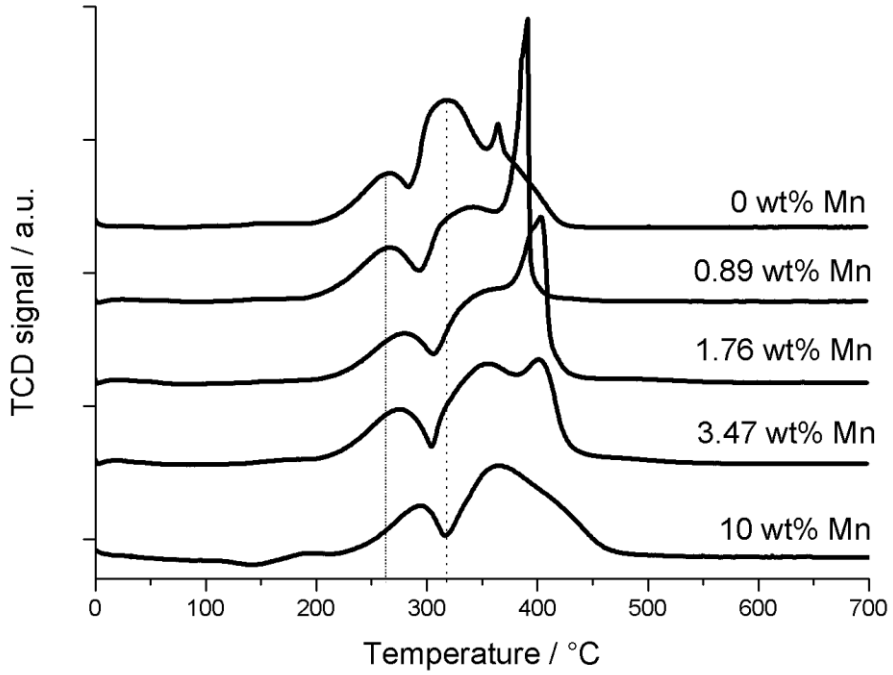

Figure 7: TPR of Co_3O_4 nanoparticles with different manganese loadings.

The sample with highest Mn loading was reduced under hydrogen and analysed by XRD **(Figure 8)**. Under hydrogen gas at 425 °C, cobalt oxide was reduced completely to metallic $Co^{(0)}$, whilst manganese (III and IV) oxide species were reduced to MnO. In general, for supported materials, cobalt metal and MnO are reported to be formed after reduction and no metallic Mn was observed.[33]

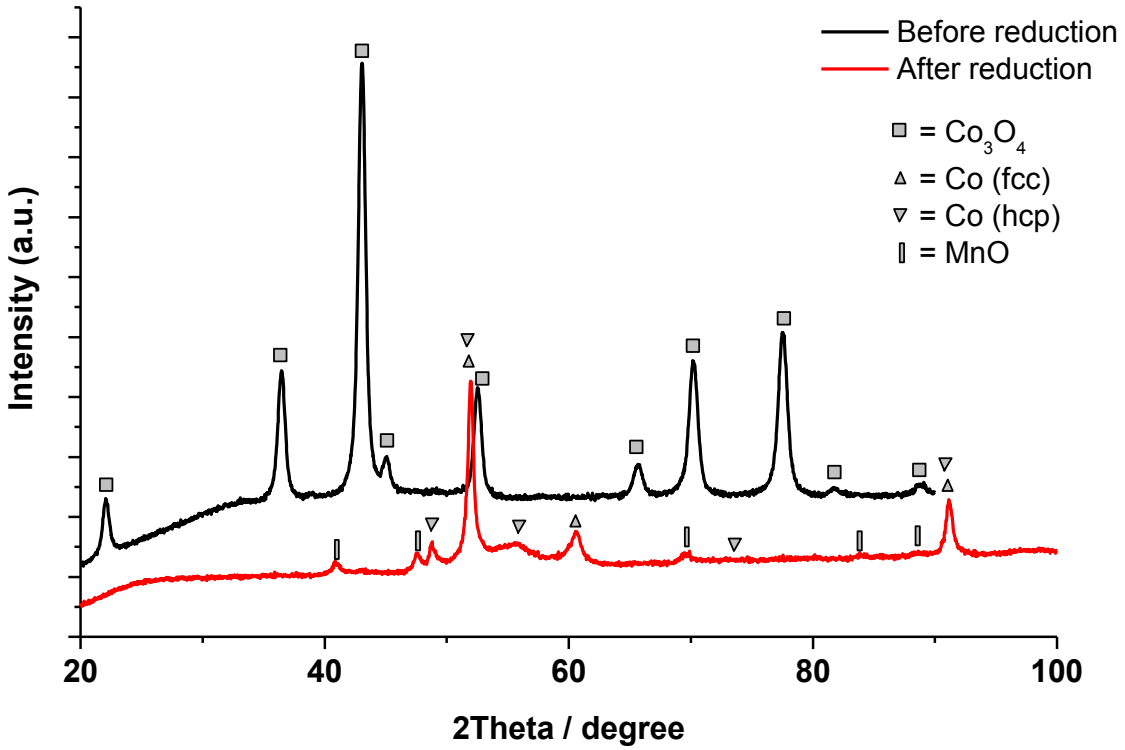

Figure 8: X-ray diffractogram of (10 wt % Mn on Co_3O_4), before (black), and after reduction (red).

3.5 Water oxidation activity of cobalt oxide and manganese modified cobalt oxide nanoparticles

Water oxidation represents half of the water splitting reaction and has important applications in artificial photosynthesis approaches to renewable energy and solar fuel production.[39] The water oxidation reaction is analogous to that found in the Photosystem II of plant photosynthesis:

$$2H_2O + 4h\nu \rightarrow O_2\uparrow + 4H^+ + 4e^-$$

Potentially the protons released can be readily reduced to H_2, or electrons used for reduction of CO_2 into products such as methanol or methane.[40,41] Artificial

photocatalyzed water oxidation utilizes a light absorbing photosensitizer (typically $Ru(bpy)_3^{2+}$), an electron acceptor capable of extracting an electron from the excited state sensitizer, and a catalyst.[42] For water oxidation to occur at the surface of metal oxide catalysts, four successive oxidations need to take place, with splitting of the water commencing at the fourth MO^{4+} state. Oxides of iridium or ruthenium are known to be effective in water oxidations,[41] however more recently cobalt oxide has been found to be an effective low cost catalyst.[43,44,45,46,47] In addition, MnO_x species has been reported to enhance the water oxidation ability of cobalt oxide.[48, 49, 50] We therefore investigated first the effect of particle size of cobalt oxide and further the presence of Mn on water oxidation ability of Co_3O_4.

Reactions using Co_3O_4 catalyst samples of 11 nm, 16 nm and 22 nm size indicated that the 11 nm nanoparticles gave the highest TOF of $1.25 \times 10^{-3}\ s^{-1}$ and O_2 generation rate over 5 to 15 min of reaction time after light on (**Figure 9i**). This was followed by the 16 nm and 22 nm sample, most likely due to relative surface area of these samples. A similar effect has been reported by M. Grzelczak et al.[51] wherein the amount of oxygen evolved increased with decreasing particle size. A comparison of photocatalytic water oxidations using nanoparticles in terms of O_2 yield, generation rates, TOF and Φ is shown in **Table 2.** It should be noted that the pentamine cobalt liberates ammonia upon its irreversible electron acceptance from the excited state $[Ru(bpy)_3]^{2+*}$,[52, 53] with high reaction rate the pH of the reaction rises rapidly to levels at which the sensitizer becomes unstable which can result in premature cessation of the water oxidation reaction. Profiles obtained with the 11 nm samples tended to show fluctuations in O_2 output due to instability induced by the initial high reaction rate. This may well account for the higher overall O_2 yield of 113 µmol obtained at longer reaction

time with the 22 nm sample, as the slower initial reaction rate allowed more stable and sustained reaction to take place at longer reaction time.

Further the presence of Mn on the water oxidation property of cobalt oxide was studied (**Figure 9ii**). O_2 yields increased with increasing Mn content up to 1.76 wt%, the highest Quantum yield (Φ) of 14.5 % and maximum oxygen yield of 118 µmol was also obtained with this sample. This is 98% of the maximum theoretical yield of 120 µmol based on electron acceptor concentration. However the highest reaction rate during the time period of 5 to 15 min and highest TOF was obtained at 3.47 wt% Mn. Overall under the reaction condition used, higher O_2 yields and initial generation rates up to 30% higher were obtained with samples containing Mn at a few wt % and above, compared to the pure Co_3O_4 samples (**Figure 9ii inset**). With further increase in manganese loading to 10 wt% no increase in the catalytic activity was observed. The catalytic activity is dependent on the binding strength of the intermediates to the metal oxide site. Substitution of octahedral cobalt sites with other elements can affect this binding strength. Y. Zhang et al. [48] reported that the oxidation state of the doping element plays a crucial role in altering the activity. Mn with higher average oxidation state of 3.7^+ can bind strongly to oxygen resulting in poor water oxidation activity. Whereas if the substituted Mn is in a lower average oxidation state such as 3.1^+, it can enhance the water oxidation activity. In our case, an enhancement of activity is seen at all loadings compared to a Mn-free cobalt oxide catalyst suggesting Mn is in an optimal favourable oxidation state for oxygen binding. However, saturation is reached and the enhancement in activity is not increased at loadings higher than 3.5 wt %.

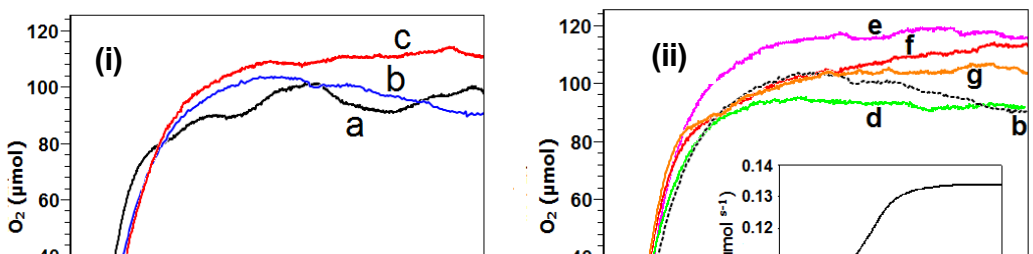

Figure 9 : Graphs of O_2 generation for photocatalytic water oxidation reactions utilizing $[Ru(bpy)_3]^{2+}$, $[Co(NH_3)_5Cl]^{2+}$ (electron acceptor) and 10 mg of Co_3O_4 catalyst suspended in N_2 degassed aqueous acetate buffer solution at initial pH 5.2

(i) using Co_3O_4 of size (a) 11 nm, (b) 16 nm and (c) 22 nm

(ii) using 16 nm Co_3O_4 with (d) 0.89 wt % Mn, (e) 1.76 wt % Mn, (f) 3.47 wt % Mn, (g) 10 wt % Mn. Dotted line shows Mn free 16 nm Co_3O_4 for comparison. Inset shows O_2 generation over 5 to 15 min of reaction time compared to Mn content of the catalyst samples.

Table 2. Summary of water oxidation activity of cobalt oxide nanoparticles (using $[Ru(bpy)_3]^{2+}$ as the light harvester dye component, $[Co(NH_3)_5Cl]^{2+}$ as the electron acceptor) showing effect of cobalt oxide size and Mn loading (SA = BET surface area m^2/g).

Co_3O_4 Sample	Max O_2 (μmol)	Average O_2 rate t=5-15min/ μmol s^{-1}	O_{2max}/ μmol s^{-1}	TOF_{max} $(x10^{-3})/s^{-1}$	ΦO_2% (at t = 45min)
(a) 11nm (SA=86)	101	0.1300	0.156	1.25	12.4
(b) 16nm (SA=64)	103	0.0995	0.119	0.95	13.0
(c) 22nm (SA=49)	113	0.0972	0.121	0.97	13.6
(d) 16nm + 0.89wt% Mn	95	0.1034	0.124	0.99	11.9
(e) 16nm + 1.76wt% Mn	118	0.1233	0.153	1.23	14.5
(f) 16nm + 3.47wt% Mn	113	0.1339	0.171	1.37	13.1
(g) 16nm + 10wt% Mn	106	0.1281	0.156	1.25	12.9

4. Conclusions

Cube-like Co_3O_4 nanoparticles have been synthesised in three different sizes using a high yielding, surfactant free method. The most significant reaction parameters that control particle size and morphology were the concentration of cobalt salt used and time of reaction. The effect of size of these unsupported cobalt oxide nanoparticles on its reduction to metallic cobalt was investigated and showed that the smaller particles were easier to reduce than their larger counterparts.

By depositing manganese on well defined, unsupported cobalt oxide nanoparticles it has been possible to probe the relationship between promoter metals and cobalt oxide without any of the complications associated with a commercial supported catalyst system, such as support interactions and variable crystallite size and shape. XPS was able to detect manganese, which was surface enriched and in a mixture of the III and IV oxidation states. The intensity of the Mn 2p XPS spectrum increased linearly with increasing manganese loading, and manganese was not detected by XRD. This implies that manganese is well dispersed or in the form of a thin surface layer oxide, which may be a mixed Mn-Co spinel oxide (i.e. $Mn_xCo_{3-x}O_4$) although we cannot definitively confirm this at low manganese loadings. TPR peaks were broadened and shifted to higher temperatures when manganese was incorporated. This effect was amplified by higher manganese loadings. These results not only provide valuable insight into the relationship between manganese and cobalt after calcination and reduction, but also demonstrate the inhibitive effect that manganese has on cobalt oxide reduction.

The nanoparticles were shown to be effective metal oxide catalysts for visible light photocatalyzed water oxidations. For Co_3O_4 samples higher reaction rates were obtained with the higher surface area nanoparticles. Mn content at 1.79% and above was shown to increase both reaction rates and O_2 yields compared to pure Co_3O_4 samples.

Acknowledgements

The authors thank Natasha Bennett for help with zeta potential measurements.

Conflict of interest

All the authors certify that there is no conflict of interest to declare.

---

5. References

[1] Lignier P, Bellabarba RM, Tooze RP (2012) Chem Soc Rev 41:1708

[2] Moshfegh AZ (2009) J Phys D Appl Phys 42, 23**:**233001

Cuenya BR (2010) Thin Solid Films 518:3127

[3] Fischer N, Clapham B, Feltes T, E. van Steen, Claeys M (2014) Angew Chem Int Ed 53:1342

[4] Beaumont SK (2014) Phys Chem Chem Phys 16:5034

[5] Mistry H, Behafarid F, Bare SR, Cuenya BR (2014) ChemCatChem 6:348

[6] Westrate CJ, Saib AM, Niemantsverdriet JW (2013) Catal Today 215:2

[7] Zaera F (2013) ChemSusChem 6, 10:1797

[8] Zaera F (2013) Chem Soc Rev 42:2746

[9] Papaefthimiou V, Dintzer T, Lebedeva M, Teschner D, Haveker M, Knop-Gerike, Schlogl R, Pierron-Bohnes B, Savinova E, Zafeiratos S (2012) J Phys Chem C 116**:**14342

[10] Zheng F, Alayoglu S, Pushkarev VV, Beaumont SK, C. Specht, F. Aksoy, Z. Liu, J. Guo, G. A. Somorjai (2012) Catal Today 182:54

[11] Morales F, de Smit E, de Groot FMF, Visser T, Weckhuysen BM (2007) J Catal 246:91

[12] Morales F, De Groot FMF, Gitzel P, Kleimenov E, Bluhm H, Havecker M, Knop-Gericke A, Weckhuysen BM (2004) J Phys Chem B 108:16201

[13] Khodakov AY, Lynch J, Bazin D, Rebours B, Zanier N, Moisson B, Chaumette P (1997) J Catal 168:16

[14] Li YG, Tan B, Wu YY, (2008) Nano Lett 8:265

[15] Geng B, Zhan F, Fang C, Yu N (2008) J Mater Chem 18:4977

[16] Xie X, Li Y, Liu Z.-Q, Haruta M, Shen W (2009) Nature 458:746

Tuysuz H, Comotti M, Schuth F (2008) Chem Comm 4022

Davies TE, Garcıa T, Solsona B, Taylor SH (2006) Chem Comm 3417

Zafeiratos S, Dintzer T, Teschner D, Blume R, Hävecker M, Knop-Gericke A, Schlögl R (2010) J. Catal 269:309

[17] Khodakov AY, Chu W, Fongarland P (2007) Chem Rev 107:1692

[18] Shao Y, Sun J and Gao L (2009), J Phys Chem C 113:6566
Wang G, Shen X, Horvat J, Wang B, Liu H, Wexler D, Yao J (2009) J Phys Chem C, 113:4357
Lai T-L, Lai Y-L, Lee C-C, Shu Y-Y, Wang C-B (2008) Catal Today 131:105.
Wen-hui Li (2008) Materials Letters 62:4149
Xu C, Sun J, Gao L (2011) CrystEngComm, 13:1586

[19] Lestera E, Aksomaityte G, Lia J, Gomeza S, Gonzalez-Gonzaleza J, Poliakoff M (2012) Progress in Crystal Growth and Characterization of Materials, 58:3

[20] Feng J, Zeng HC (2003) J Phys Chem B 107:926
Feng J, Zeng HC (2003) Chem Mater 15:2829

[21] Morales F, Weckhuysen BM (2006) Catalysis 19:1

[22] Morales F, de Smit E, de Groot FMF, Visser T, Weckhuysen BM (2007) J. Catal, 246:91

[23] Miyazawa T, Hanaoka T, Shimura K, Hirata S (2013) Applied Catalysis A: General, 467:47

[24] Werner S, Johnson GR, Bell AT (2014) ChemCatChem 6:2881

[25] Thiessen J, Rose A, Meyer J, Jess A, Curulla-Ferré D (2012) Microporous and Mesoporous Materials 164:199

[26] Walsh D, Sanchez-Ballester NM, Ariga K, Tanaka A and Weller M (2015) Green Chemistry 17:982

[27] Potoczna-Petru D, Kepinski L (2001) Catalysis Letters 73:41 and references therein

[28] O. A. Bulavchenko, S. V. Cherepanova, V. V. Malakhov, L. S. Dovlitova, A. V. Ishchenko, S. V. Tsybulya (2009) Kinetics and Catalysis 50:192

[29] Y. Ji, Z. Zhao, A. Duan, G. Jiang, J. Liu (2009) J. Phys. Chem. C, 113:7186

[30] H. Li, J. Li, H. Ni, D. Song (2006) Cat. Lett. 110:71
R. Bechara, D. Balloy, J. Dauphin, F. Grimblot (1999) Chem. Mater. 11:1703
A. Y. Khodakov, J. Lynch, D. Bazin, B. Rebours, N. Zanier, B. Moisson, P. Chaumette (1997) J. Cat. 168:16

[31] A. Martínez, C. López, F. Márquez, I. Díaz (2003) Journal of Catalysis 220:486

[32] V. B. R. Boppana, F. Jiao (2011) Chem. Commun. 47:8973

[33] F. Morales, D. Grandjean, F. M. F. de Groot, O. Stephan, B. M. Weckhuysen (2005) Phys. Chem. Chem. Phys. 7:568

[34] M. J. Keyser, R. C. Everson, R. L. Espinoza (1998) Appl. Catal. A: Gen. 171:99

[35] Qi Liang, K. Chen, W. Hou, Q. Yan (1998) Applied Catalysis A: General 166:191. N. Ahmad, S. T. Hussain, B. Muhammad, N. Ali, S. M. Abbas, Y. Khan (2013) Bull. Korean Chem. Soc. 34:3005.

[36] H.E. Barner, C.L. Mantell (1968) Industrial & Engineering Chemistry Process Design and Development 7:285

[37] F. Morales, D. Grandjean, Ad Mens, F. M. F. de Groot, B. M. Weckhuysen (2006) J. Phys. Chem. B 110:8626

[38] T. E. Feltes, L. Espinosa-Alonso, E. De Smit, L. D'Souza, R. J. Meyer, B. M Weckhuysen, J. R. Regalbuto (2010) J. Cat. 270:95

[39] T. Faunce, S. Styring, M. R. Wasielewski, G. W. Brudvig, A. W. Rutherford, J. Messinger, A. F. Lee, C. L. Hill, H. deGroot, M. Fontecave, D. R. MacFarlane, B. Hankamer, D. G. Nocera, D. M. Tiede, H. Dau, W. Hillier, L. Wang, R. Amal (2013) Energy Environ. Sci 6:1074

[40] C. Herrero, A. Quaranta, W. Leibl, A. W. Rutherford, A. Aukauloo (2011) Energy & Environmental Science, 4:2353

[41] F. E. Osterloh, B. A. Parkinson (2011) MRS Bulletin 36:17

[42] M. Hara, C. C. Waraksa, J.T. Lean , B. A. Lewis, T. E. Mallouk (2000) The Journal of Physical Chemistry A 104:5275

[43] F. Jiao, H. Frei (2009) Angewandte Chemie-International Edition 48:1841

[44] D. Shevchenko, M. F. Anderlund, A. Thapper, S. Styring (2011) Energy & Environmental Science 4:1284.

[45] J. Guan, C. Ding, R. Chen, B. Huang, X. Zhang, F. Fan, F. Zhang, Can Li, (2017) Chemical Science 8:6111

[46] K. Maeda , K. Ishimaki, M. Okazaki, T. Kanazawa, D. Lu, S. Nozawa, H. Kato, M. Kakihana (2017) ACS Appl. Mater. Interfaces 9:6114

[47] Z. Chen, S. Miao, J. Guan, F. Zhang, C. Li (2016) Applied Catalysis A: General 521:154

[48] Y. Zhang, J. Rosen, G. S. Hutchings, F.Jiao (2014) Catalysis Today 225:171

[49] F. Jiao, H. Frei (2010) Chem. Commun. 46:2920

[50] Liu, H. and G. R. Patzke (2013) Nanostructured Materials and Nanotechnology VII, John Wiley & Sons, Inc. 75.

[51] M. Grzelczak, J.S. Zhang, J. Pfrommer, J. Hartmann, M. Driess, M. Antonietti, X.C.Wang (2013) ACS Catal. 3:383

[52] L. Duan, Y. Xu, P. Zhang, M. Wang, L. Sun (2010) Inorganic Chemistry 49:209

[53] D. Walsh, N. M. Sanchez-Ballester, K. Ariga, A.Tanaka, Mark Weller (2015) Green Chemistry 17:982